Supporting Information

An Aqueous Hybrid Electrolyte for Low-Temperature Zinc-Based Energy Storage Devices

Nana Chang,[ab] Tianyu Li,[a] Rui Li,[ab] Shengnan Wang,[ab] Yanbin Yin,[a] Huamin Zhang[a] and Xianfeng Li*[a]*

[a.] Division of Energy Storage, Dalian National Laboratory for Clean Energy, Dalian Institute of Chemical Physics, Chinese Academy of Sciences, 457 Zhongshan Road, Dalian 116023, China.
[b.] University of Chinese Academy of Sciences, Beijing 100049, China.

Experimental section

Synthesis of cathode materials: All chemicals and reagents were of analytical grade and used without further purification. The activated carbon (AC) was purchased from AC, Song Ya Chemical (Shanghai) Co., Ltd; Active Carbon 600-1000. The N-doped activated carbon (NAC) was achieved by annealing the AC sample at 900 °C for 4 hours under a NH_3 flow with a heating rate of 5 °C min^{-1} in the tubular furnace. The zinc-ion intercalation compound, PANI-intercalated V_2O_5 composite, was fabricated using a facile hydrothermal method. Typically, 0.72 g of V_2O_5 powder was dissolved in a mixture solution containing 60 mL of DI water,10 mL of H_2O_2 (30 wt. %) to obtain a homogeneous clear orange solution. Keep it sealed into a 100 mL Teflon-lined stainless steel autoclave and heated at 190 °C for 10 h to produce the hydrated V_2O_5 hydrogel. The PANI-intercalated V_2O_5 composite was synthesized by vigorously stirring the prepared hydrated V_2O_5 hydrogel with aniline monomers at room temperature. During the process, dark blue precipitate can be produced. Isolate and wash the precipitate by filtration with DI water for several times, followed by getting freeze-dried under −40 °C for 24 h to obtain the final product.

Preparation of electrodes and assembly of full cell: AC and NAC electrode were prepared by mixing AC or NAC with conductive agent of Ketjen Black (KB), binder of polytetrafluoroethylene (PTFE) in a mass ratio of 8:1:1. The mixture was dispersed in

isopropanol to form a paste, and then rolled into a film electrode. After being dried at 60 °C overnight, the film was cut into circular pieces with size of Φ10 mm. The cathode electrode was finally obtained by pressing the circular pieces onto Ti net (size Φ14 mm). The V_2O_5 cathode was fabricated by mixing V_2O_5 with super P and polyvinylidene fluoride (PVDF) at the weight ratio of 7:2:1 and dissolving above mixture in an appropriate amount of N-methyl-2-pyrrolidone (NMP) to form a slurry. The slurry was stirred vigorously for 5 hours and then spread onto stainless steel mesh, dried in vacuum oven at 70 ^oC overnight. The mass loading of above active materials (both AC/NAC and V_2O_5) was about 2.5~3.0 mg cm^{-2}. The electrolytes were obtained by dissolving zinc sulfate heptahydrate into the EG-water binary solvents to form a Zn^{2+} salt solution of 2 mol L^{-1}. In the mixed solvents, the volume content of EG was increased gradually from 0% to 5%, 20%, 40%, 60 % in water. And the relevant electrolytes were marked as EG0, EG5, EG20, EG40, and EG60 respectively. Full cells were assembled in CR2025-type coin cells at air atmosphere, using zinc foil (50 μm) as anode and glass fiber filter (Whatman, grade GF/A) as the separator.

Materials characterization: The apparent viscosity of the electrolyte at specified temperature can be obtained with rotational viscosity test with a rotary rheometer HAAKE MARS III (Thermofisher, USA) at various temperatures. The freezing point of the hybrid electrolytes was measured by differential scanning calorimetry (DSC) through a NETZSCH STA 449 F3 Instrument (Germany). Sample of 10mg for an electrolyte was sealed in a pre-weighed aluminum sample pan with a NETZSCH sealing press. A same pre-weighed aluminum sample pan was also sealed as the blank reference. During the measurement, the sealed pan with electrolyte was firstly cooled down to -150 ^oC at the rate of 10 ^oC min^{-1} using liquid nitrogen cooling system, then equilibrated at -150 ^oC for 10 min, finally followed with the procedure scanning from -150 ^oC to 20 ^oC at the rate of 10 ^oC min^{-1}. The freezing point of the electrolyte can be estimated by taking the peak temperature due to the unclear onset melting point. The H bonding reaction between EG and water in hybrid electrolytes were examined by FT-IR spectrometer

(Nicolet iS50, Thermofisher). Each spectrum was recorded at a rate of 32 scans with a resolution of 4 cm^{-1}, collected from 1111 to 4000 cm^{-1} in transmission mode. A liquid solution of 20 μL was tested via a CaF_2 cell sealed with screws. Raman spectra was recorded using Advantage 785 Raman spectrometer (NanoWizard Ultra Speed & inVia Raman, Germany) equipped with a HeNe laser emitting at 785 nm. The spectral resolution of the two spectrometers was 5 cm^{-1}. The spectra were collected with an accumulation time of 10 s via a glass tube filled with 400 μL electrolyte. NMR analysis was carried out on an AVANCE III 400MHz equipment (Switzerland) to further illustrate the H bonds changes in various electrolytes. A liquid sample of 400 μL was measured via the coaxial double tube where the inner tube was filled with deuterated reagent and the outer tube was filled with the sample. The deuterated reagent was used as the field frequency lock for NMR tests. Deuterated H_2O (D_2O), a common reagent, was used for room-temperature NMR test. However, once the temperature falls below 0 ºC, D_2O gets frozen. Thus, the deuterated chloroform ($CDCl_3$) with lower freezing point was used for variable-temperature NMR tests. Besides, to protect the NMR tube from damage and make sure that the liquid sample cannot freeze during the variable-temperature NMR test, EG40, as an example, was used for this test due to its wide range of varying temperatures. The morphologies of zinc deposition for different electrolytes were obtained by field-emission scanning electron microscopy (FE-SEM, JEOL 6360LV, Japan). The Powder X-ray diffraction (XRD) patterns were recorded with a 2θ range of 5º to 80º using an X-ray diffractometer (D8 ADVANCE ECO; RIGAKU, Japan) equipped with Cu-Kα radiation source at 40 kV and 40 mA and scan rate of 10 º min^{-1}, and the electrode characterization was obtained by ex-situ XRD. It should be mentioned that all the cathodes, after being charged or discharged to certain potentials, were washed with distilled water to get rid of electrolyte residual and dried in a vacuum freezing dryer before physical characterization. The pore size distribution of AC/NAC was analyzed by the Brunauer-Emmett-Teller surface area analyzer (ASAP 2020, Micromeritics). The weight changes of the hybrid electrolytes in air condition were

measured by weighing the electrolytes after resting in air for an interval of 12 hours at 25 ^{o}C. The flammability tests of the hybrid electrolytes were carried out by igniting the hybrid electrolyte-soaked glass fiber membranes for 10 seconds.

Electrochemical test: The ionic conductivity of the hybrid electrolytes was measured at different temperatures through electrochemical impedance spectroscopy (INTERFACE1000, Gamry, USA) with cells consisted of two parallel Pt-plate electrodes (1 cm×1 cm). The applied frequency range was from 1000 Hz to 0.1 Hz with an AC amplitude of 10 mV. The electrolyte resistance was acquired from the intercept of Nyquist plot and the ionic conductivity was calculated according to the following equation:

$$\sigma = G\frac{L}{A} = \frac{L}{R_s A} \quad (1)$$

Where σ (S cm^{-1}) is the per unit conductivity, G (S) is conductance, R_s is the electrolyte resistance, L (cm) is interval distance (1 cm) between the two Pt-plate electrodes, A (cm^2) is electrode area.[1]

All the tests were carried out after samples being maintained at the specified temperature for 2 hours. The linear sweep voltammetry (LSV) of the hybrid electrolytes at a scan rate of 10 mV s^{-1} was examined with a two-electrode system where glassy carbon was used as working electrode and zinc foil as counter electrode (INTERFACE1000, Gamry, USA). Cyclic voltammetry (CV) tests for Zn^{2+}/Zn anode and AC cathode were conducted with a three-electrode system in 2 M $ZnSO_4$ solution where glassy carbon and AC cathode were used as working electrodes respectively, Pt plate as counter electrode, and saturated calomel electrode (SCE) as reference electrode through a VMP3 multi-channel electrochemical workstation (BioLogic, France). Besides, the CV curves of full cell were measured by a two-electrode system in the hybrid electrolytes where the AC electrode was used as working electrode and zinc foil as counter electrode. These capacitive effects were characterized by analyzing the cyclic voltammetry curves at various sweep rates according to the power-law equation:

$$i = av^b \quad (2)$$

Where i (A g^{-1}) is the sum of the capacitive-controlled current (i_c) and diffusion-controlled current (i_d); v (mV s^{-1}) is the scan rate; the value of b is determined by the slope of linear log(i)-log(v). In general, if b-value is 0.5, the energy storage process is controlled by diffusion, while 1.0 indicates a surface capacitance-controlled process. Hence, the calculated b value in this work is around 0.8, which implies that the energy storage process is controlled by the diffusion and capacitive behavior synergistically.[2] Specific contributions from each process can be quantified by the following equations:

$$i(V) = i_c + i_d = k_1 v + k_2 v^{1/2} \quad (3)$$

Equation (3) can be transformed to Equation (4):

$$i(V)/v^{1/2} = k_1 v^{1/2} + k_2 \quad (4)$$

According to Equation (4), the values of k_1 and k_2 can be acquired by reading the slope and intercept from the curves of linear $i/v^{1/2}$- $v^{1/2}$, and thereby both charge storage contributions are obtained though multiplying the k-value by v and $v^{1/2}$ respectively.[2]

Symmetric Zn||Zn cells were assembled to explore the long-term cycling stability of zinc metal anodes in the hybrid electrolytes with a charge capacity of 1 mA h cm^{-2} at a current density of 2 mA cm^{-2}. Also, similar Ti||Zn cells were carried out to analyze the coulombic efficiency for zinc plating/stripping process. The symmetric and full battery performance were performed by a LANHE battery charge/discharge system of CT3001A series (China). Zinc-ion hybrid supercapacitors (ZHSCs) and zinc-ion batteries (ZIBs) were investigated at the current densities ranging from 0.2 to 20 A g^{-1} at certain temperature (20/0/-10/-20/-30/-40 ^{o}C) for rate performance test, and 0.2 A g^{-1} at -20 ^{o}C for cycling test. Low-temperature battery tests were conducted though a programmable constant temperature and humidity test chamber (ZKMD-LS-225H, Dalian). The self-discharge behaviors of EG0 and EG40 were tested at a current density of 0.5 A g^{-1} and the rest time is 24 hours.

The energy (E [Wh kg^{-1}]) and power densities (P [W kg^{-1}]) of the batteries were calculated based on active materials as follows:

$$E = C \times V_m \quad (5)$$

$$P = I \times V_m \tag{6}$$

Where C (mA h g^{-1}) is the specific capacity，I (A g^{-1}) is the current density, and V_m (V) is the midpoint discharge voltage.

Computational details

Molecular dynamics simulations: Molecular dynamics (MD) simulations were carried out using LAMMPS package to investigate the solvation structure of electrolyte.[3-9] The number of molecules for each electrolyte was listed in Table S2. The forced field parameters for EG, Zn^{2+} and SO_4^{2-} were obtained from OPLS_AA force fields. The SPC/E water model is employed for H_2O, and the bonds and the angle of water molecules were constrained with SHAKE algorithm. The velocity-verlet method was used as integral method and the integration time step was 1 fs. The cutoff radiuses for vdW and the electrostatic interactions were both 15 Å. The standard periodic boundary condition was used in all simulations. Particle-particle particle-mesh (PPPM) solver was applied to the long electrostatic interactions with a precision of 1×10^{-5}. After minimization, each system was initially equilibrated for 12 ns in NPT (isothermal–isobaric) ensemble. Nosé–Hoover thermostat/barostat algorithm were used to control the system temperature and pressure in NPT ensemble. The simulation temperature was 298.15 K and the pressure was 1 atm. After the system was fully equilibrated, another 5 ns was run to collect the date for statistical analysis in NVT ensemble. Berendsen thermostat algorithm was used to control the temperature of each system in NVT ensemble.

Quantum chemistry calculations: All structures were optimized by Density functional theory (DFT) at PBE0 hybrid functional with def2-SVP basis set, using Gaussian 16 program.[10-12] Then a single point energy calculation of each optimized structure was performed at the same hybrid functional with def2-TZVP[11] basis set. All calculations were carried out with the atom-pairwise dispersion correction (DFT-D3) and the implicit universal solvation model based on Solute Electron Density (SMD).[13-16] The Electrostatic potential (ESP) were analyzed by Multiwfn[16] package and the ESP was drawn by VMD package.[17]

Table S1. Physical properties of commonly used solvents in low-temperature energy storage systems.

Solvent	Freezing point (°C)	Boiling point(°C)	Flash point (°C)	Dielectric constant	Solubility in water[a]	Safety hazards[b]
Ethylene glycol (EG)	-12.9	197.3	111.1	37.7	Miscible	Harmful (Xn)
Dimethyl carbonate (DMC)[18]	3	90	17	3.1	13.9g/100ml	Flammable (F)
Dimethyl sulfoxide (DMSO)[19]	19	189	89	48.9	Miscible	Irritant (Xi)/F/Xn
Diethyl carbonate (DEC)[20]	-43	127	25	2.8	Insoluble	F/Xn
Acetonitrile (AN)[21,22]	-45.7	81.6	5.6	37.5	Miscible	F+/Xn
Propylene carbonate (PC)[23,24]	-48.8	242	132	65	Miscible	Xi/Xn
1,2-dimethoxyethane (DME)[25]	-58	85	-2	5.5	Miscible	Toxic(T)/F++/Xn
Dimethyl formamide (DMF)[26]	-60.5	153	58	36.7	Miscible	T/F/Xn
Ethyl Acetate (EA)[27]	-84	77	-4	6	8.3g/100ml	F/Xi/Xn
Dichloromethane (DCM)[28]	-97	40	30	9.1	1.8g/100ml	T/F/Xn
Methyl acetate (MA)[21]	-98	56.9	-10	6.7	24.5g/100ml	F+/Xi/Xn
Methyl formate (MF)[21]	-100.4	32	-19	8.5	30.0g/100ml	F+/Xn
Thionyl chloride ($SOCl_2$)[29]	-104.5	78.8	-18	-	Reacts	T+/Xn
Tetrahydrofuran (THF)[30,31]	-108.5	66	-14	7.58	Miscible	F+/T/Xi/Xn

Note: Above data comes from the corresponding references and Wikipedia. [a] Data are given for 20 °C. [b] "+" and "++" means the level of "Highly" and "Extremely", respectively.

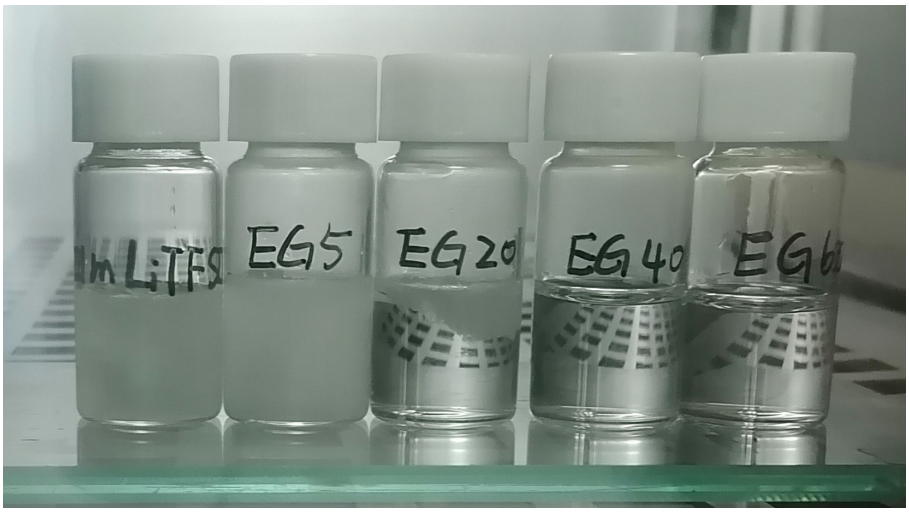

Figure S1. The snapshots of 21m LiTFSI (a typical "water-in-salt" electrolyte) and a series of hybrid electrolytes at -20 °C.

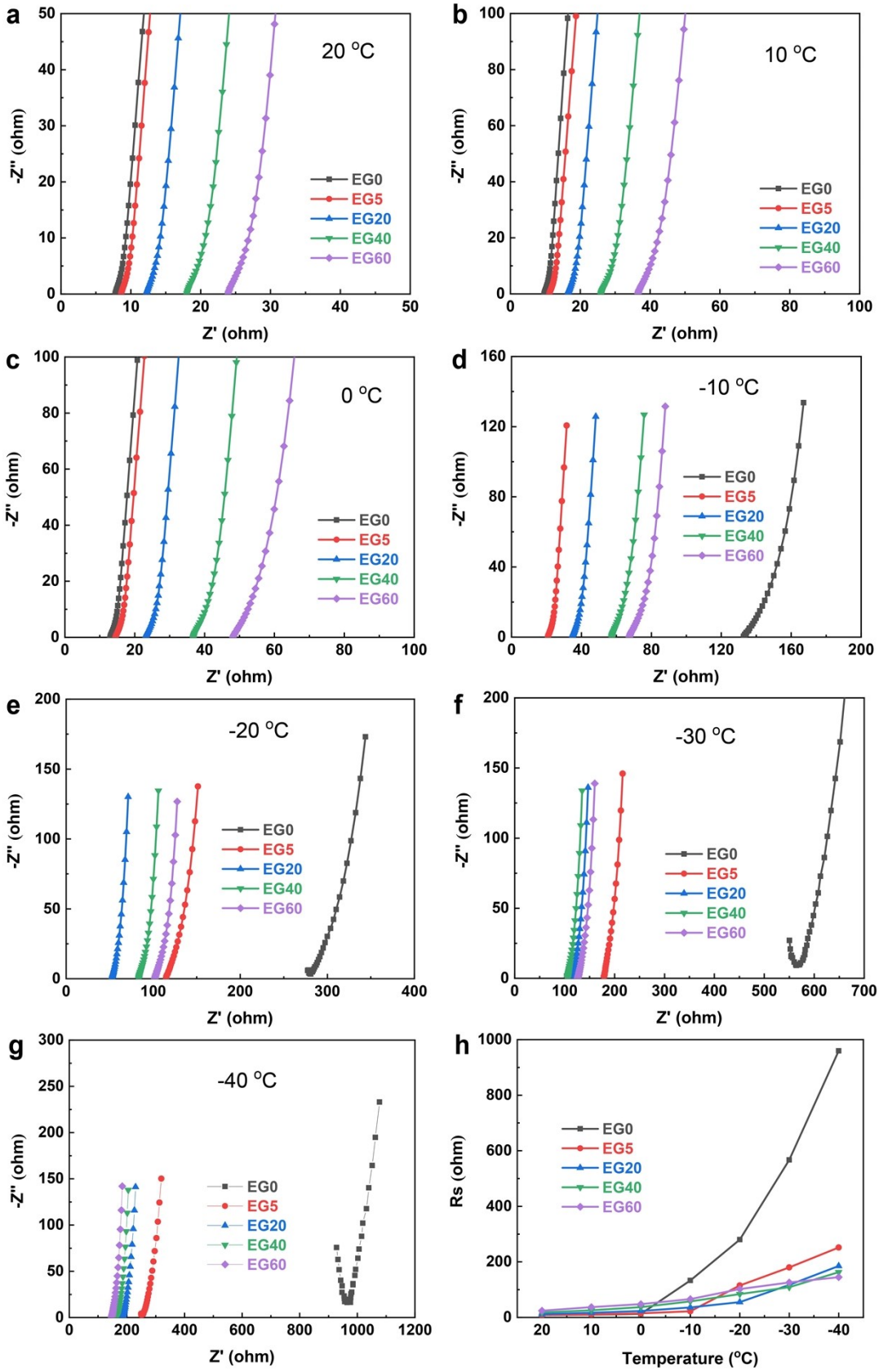

Figure S2. (a-g) Nyquist plot of electrochemical impedance spectroscopy (EIS) investigation for the hybrid electrolytes at different temperatures. (h) The resistances of

different electrolytes obtained from EIS curves.

Table S2. The specific values of the resistances (Rs) obtained from EIS curves for different electrolytes.

Hybrid electrolytes	Rs (ohm)						
	20 °C	10 °C	0 °C	-10 °C	-20 °C	-30 °C	-40 °C
EG0	8	10	13	133	280	567	960
EG5	9	11	15	22	115	180	252
EG20	12	17	23	36	55	117	185
EG40	18	26	37	58	84	109	163
EG60	24	37	48	66	102	126	145

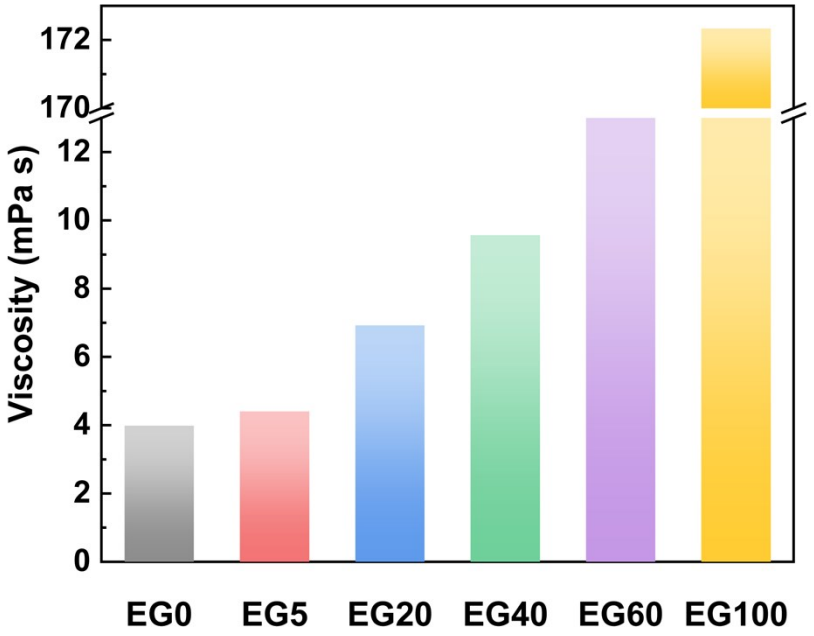

Figure S3. Viscosities of the hybrid electrolytes at 20 °C.

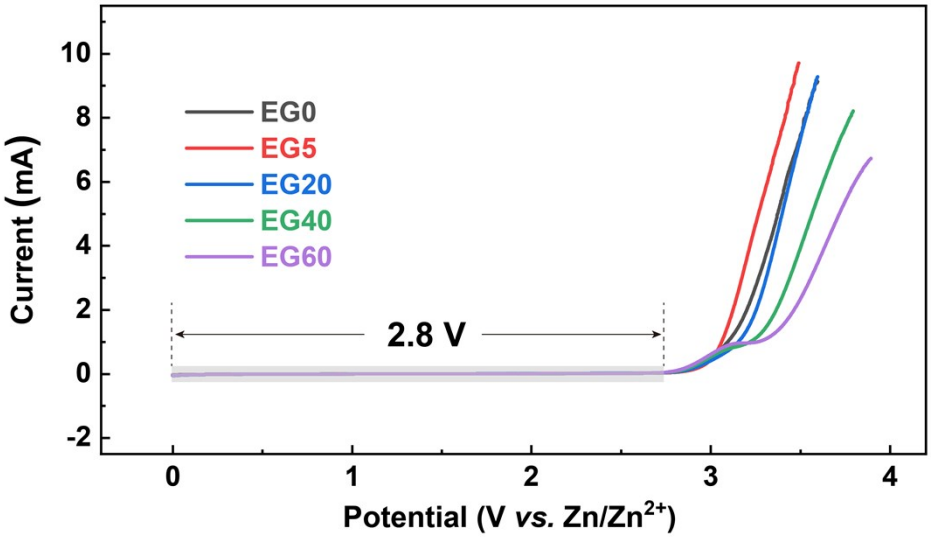

Figure S4. LSV with a scan rate of 10 mV s^{-1} for the hybrid electrolytes using glassy carbon as working electrode.

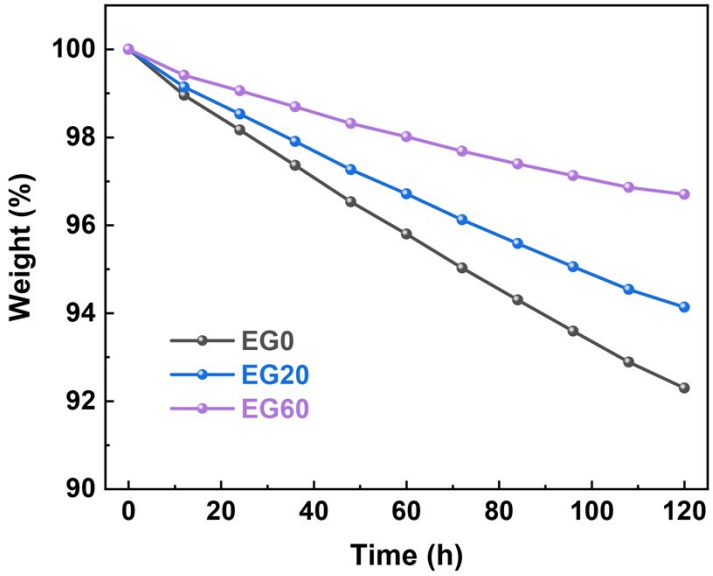

Figure S5. The weight changes of the hybrid electrolytes with different EG content in air condition.

The stability test of the hybrid electrolytes (EG0/EG20/EG60) in air condition was displayed in Figure S5. After being left in the air for some time, the weight loss of different electrolytes reveals that all the aqueous electrolytes with or without EG will volatilize in air condition. Significantly, EG can effectively decrease volatilization of the hybrid electrolytes, thus suggesting a better air stability of the hybrid electrolyte.

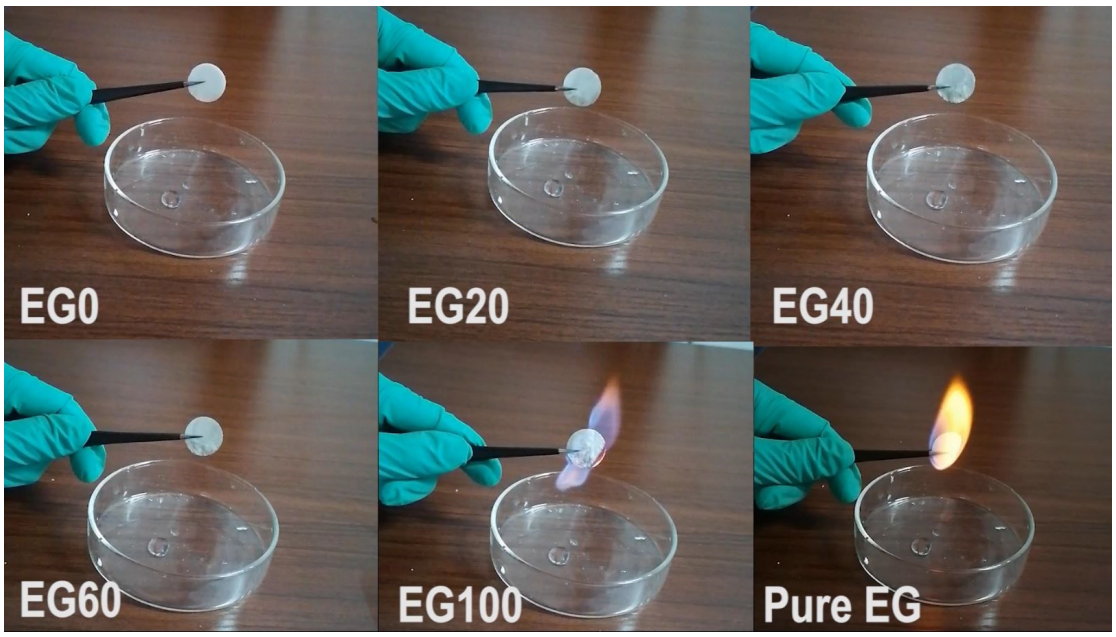

Figure S6. The snapshot from Supplementary Video 1 at about 10 s after igniting the glass fiber membranes soaked with different electrolytes.

As shown in the supplementary Video 1 and Figure S6, all the hybrid electrolytes are non-flammable even after firing the hybrid electrolyte-soaked glass fiber membranes for 10 seconds, thus confirming the high safety of this aqueous hybrid electrolytes. By contrast, EG100-soaked and pure EG-soaked glass fiber membranes were ignited, illustrating that water is essential for the low flammability of our hybrid electrolytes.

Table S3. The numbers of molecules in the hybrid electrolytes used for MD simulations.

Electrolyte	Number of $ZnSO_4$	Number of H_2O	Number of EG
EG0	100	2680	0
EG5	100	2635	45
EG20	80	1983	161
EG40	70	1542	334
EG60	60	1082	526
EG100	30	0	804

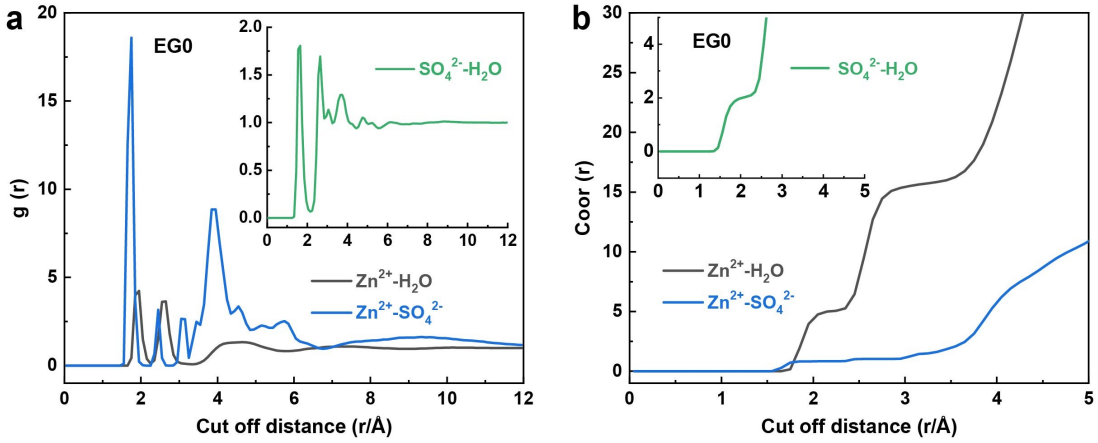

Figure S7. Radial distribution functions (RDFs) and coordination number distribution functions obtained from MD simulations for EG0 electrolyte.

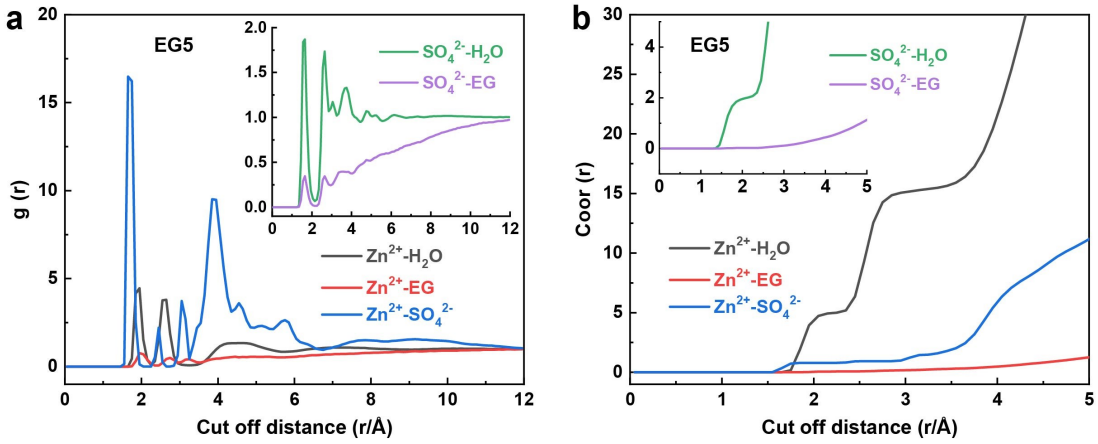

Figure S8. Radial distribution functions (RDFs) and coordination number distribution functions obtained from MD simulations for EG5 electrolyte.

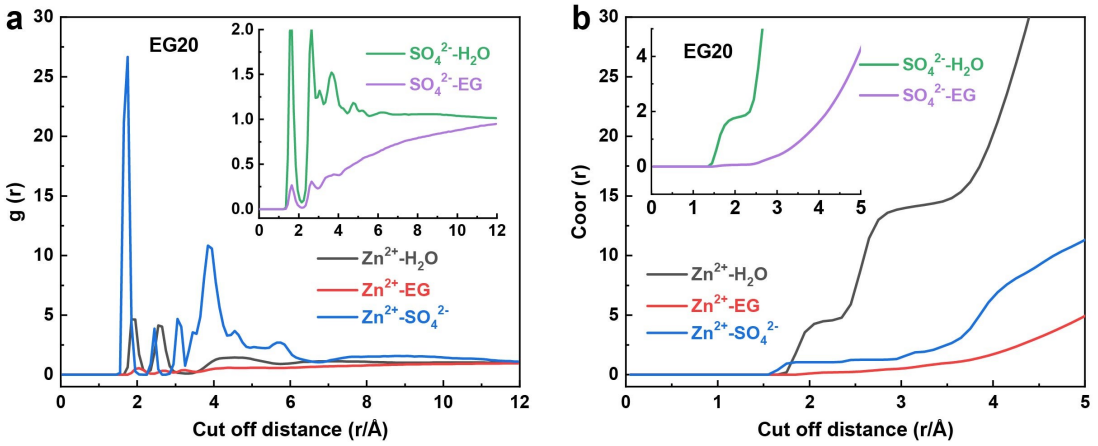

Figure S9. Radial distribution functions (RDFs) and coordination number distribution functions obtained from MD simulations for EG20 electrolyte.

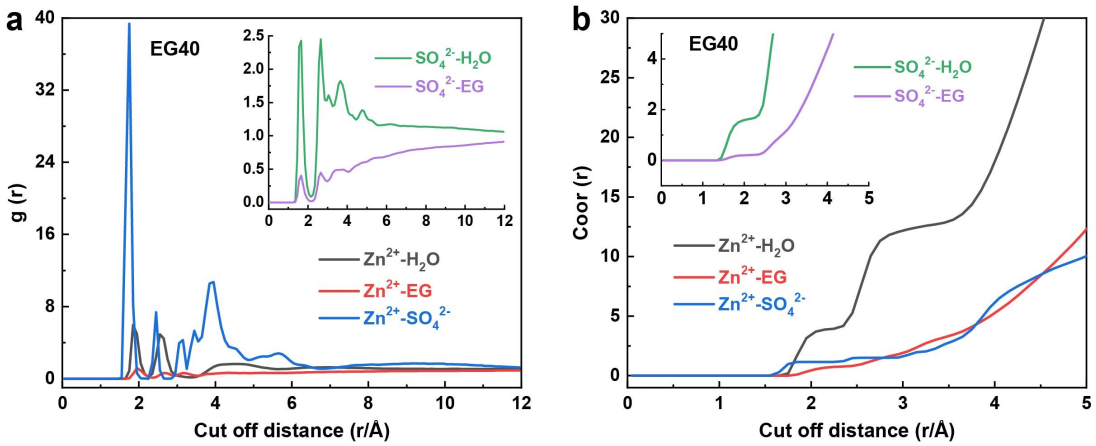

Figure S10. Radial distribution functions (RDFs) and coordination number distribution functions obtained from MD simulations for EG40 electrolyte.

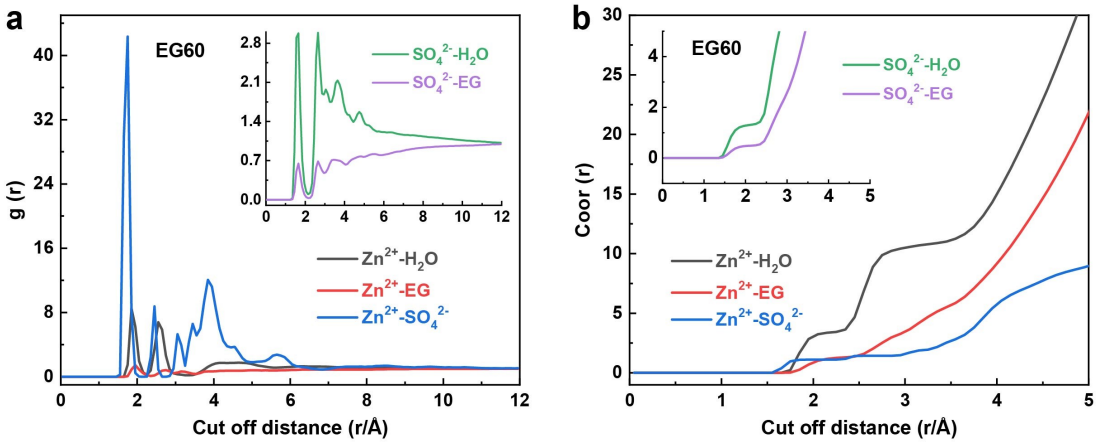

Figure S11. Radial distribution functions (RDFs) and coordination number distribution functions obtained from MD simulations for EG60 electrolyte.

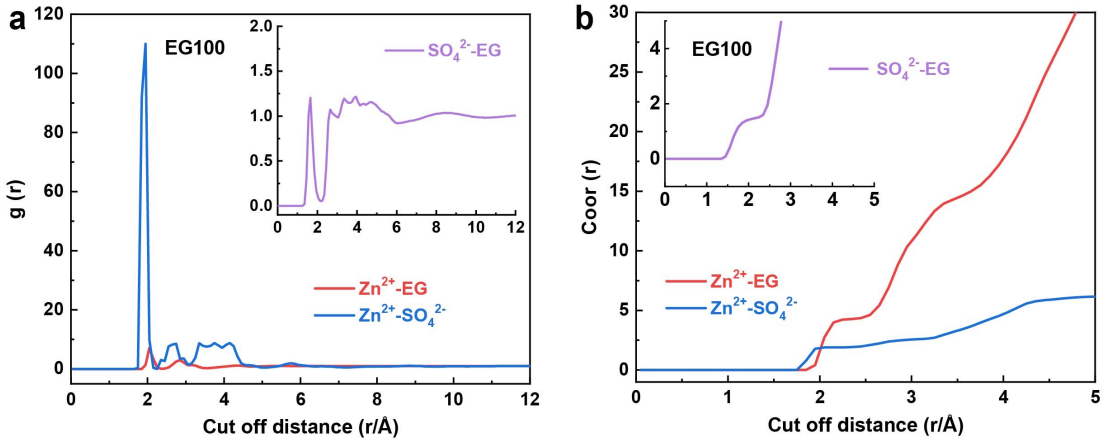

Figure S12. Radial distribution functions (RDFs) and coordination number distribution functions obtained from MD simulations for EG100 electrolyte.

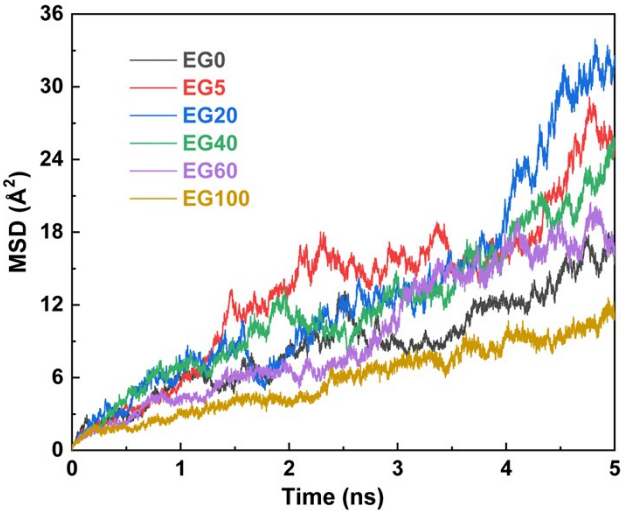

Figure S13. MSD of the Zn^{2+} in the hybrid electrolytes.

Table S4. Comparison of binding energy for Zn^{2+} with different species from DFT calculations.

System	Binding energy (kJ mol^{-1})	System	Binding energy (kJ mol^{-1})
Zn^{2+}-SO_4^{2-}	-118.03	Zn^{2+}-(1H_2O)	-59.39
Zn^{2+}-(1EG)	-63.16	Zn^{2+}-(2H_2O)	-103.27
Zn^{2+}-(2EG)	-144.75	Zn^{2+}-(3H_2O)	-136.06
Zn^{2+}-(3EG)	-199.96	Zn^{2+}-(4H_2O)	-166.47
Zn^{2+}-(4EG)	-258.34	Zn^{2+}-(5H_2O)	-169.34

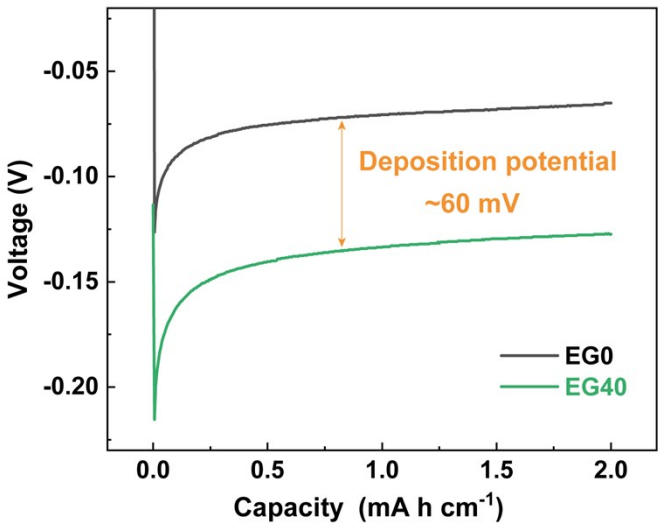

Figure S14. The potential of Zn deposition on Ti substrate at 2 mA cm^{-2}.

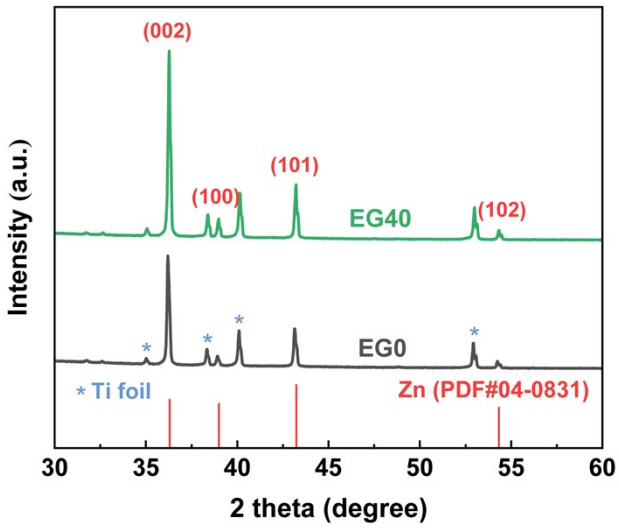

Figure S15. XRD patterns of zinc depositions.

It should be noted that the additional peaks (marked with grayish blue *) are identified as Ti mental in Figure S15 since the Zn deposits were obtained by plating a certain capacity of Zn on the Ti foil substrate via a Ti||Zn half-cell.

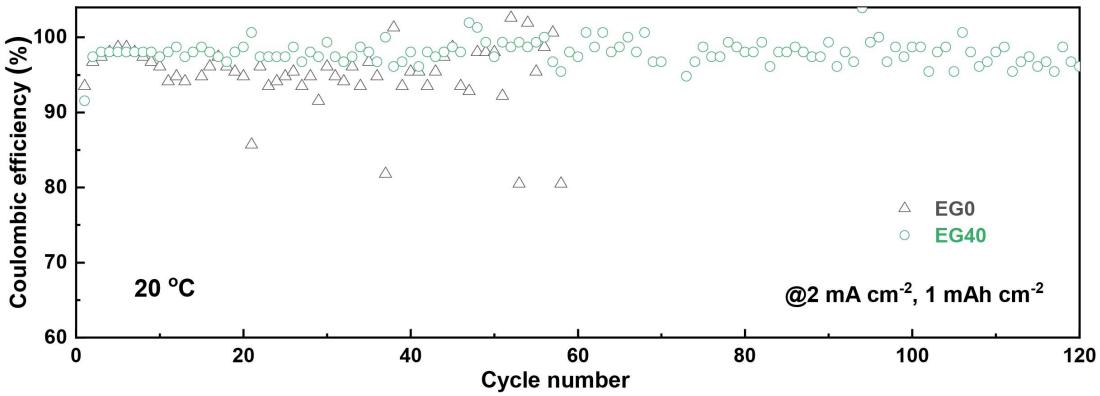

Figure S16. CE of Ti||Zn cell for EG0 and EG40 electrolytes at 20 °C.

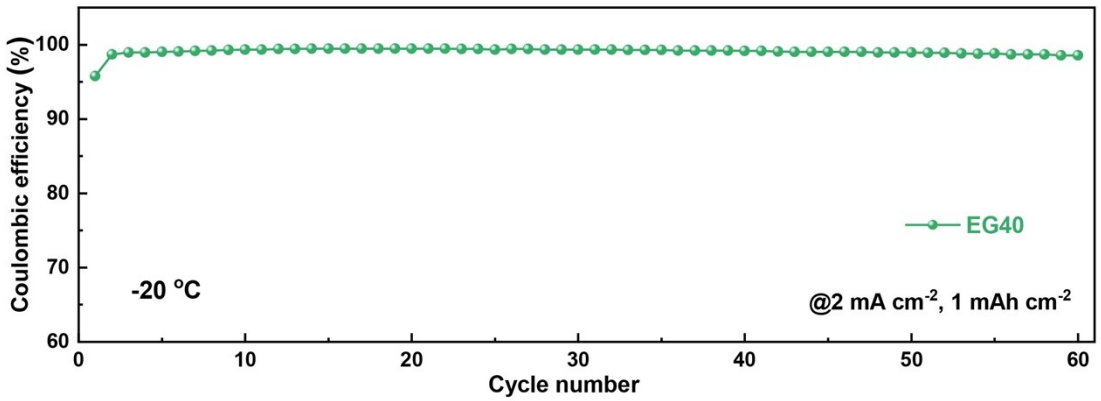

Figure S17. CE of Ti||Zn cell for EG40 electrolytes -20 °C.

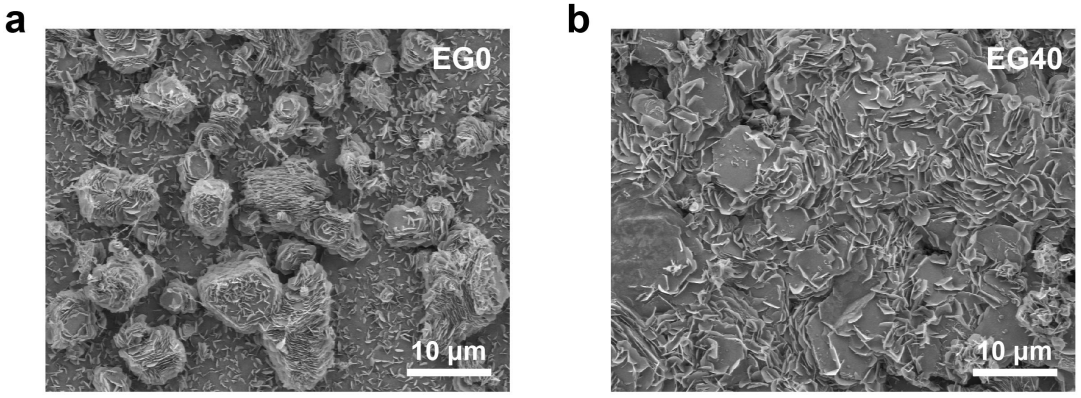

Figure S18. SEM images of zinc deposits for (a) EG0 and (b) EG40 electrolytes.

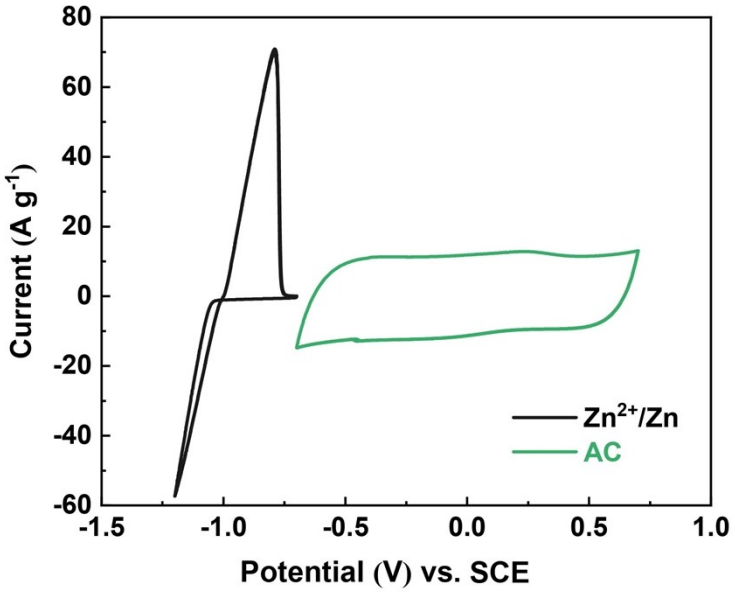

Figure S19. CV curves of the AC cathode and Zn anode in the 2M $ZnSO_4$ aqueous

electrolyte at the scan rate of 20 mV s^{-1}.

The CV curves of Zn foil anode and AC cathode were obtained through a three-electrode system in 2 M $ZnSO_4$ solution where glass carbon and AC cathode were used as working electrodes respectively, Pt plate as counter electrode, and saturated calomel electrode (SCE) as reference electrode. The results show the reversible peaks at -0.7/-1.2 V (vs. Standard Calomel Electrode (SCE)) for Zn/Zn^{2+} redox pair and the approximatively rectangular curve related to the electrochemical double layers for AC electrode.

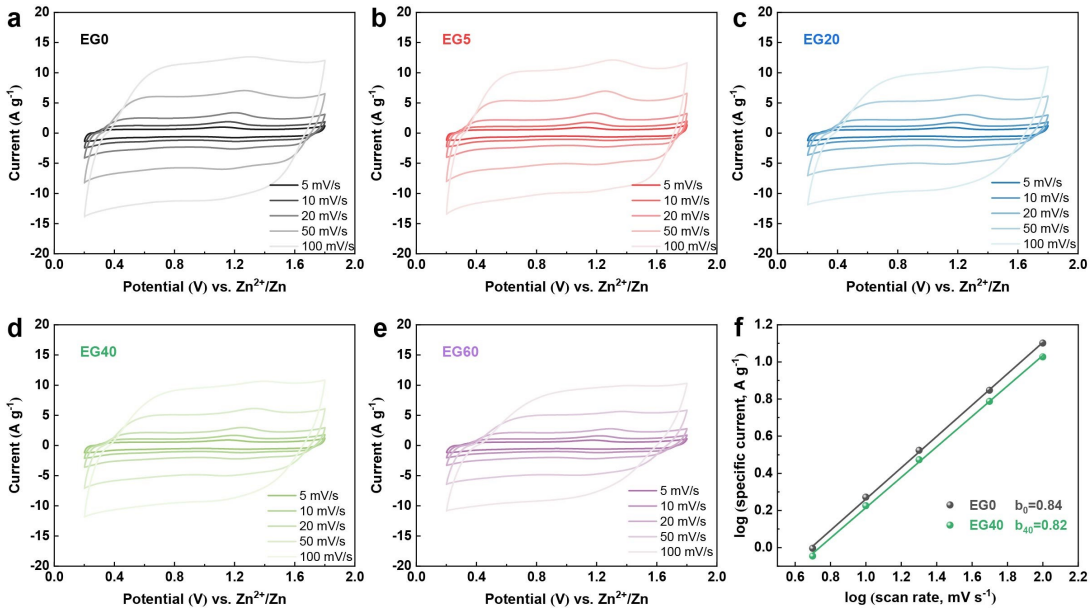

Figure S20. CV curves of (a) EG0, (b) EG5, (c) EG20, (d) EG40, and (e) EG60 electrolytes. (f) The fitting plot between log(*i*) and log(*v*) of EG0 and EG40 electrolytes.

The CV curves of full cell were evaluated in the hybrid electrolytes at scan rates of 5~100 mV s^{-1}. The b value obtained from CV curves (Figure S20f) is usually used to analyze the kinetic process. They are calculated to be 0.84 and 0.82 for EG0 and EG40 respectively, which demonstrates that the energy storage process displays the surface capacitance-dominated behavior for both electrolytes.[32]

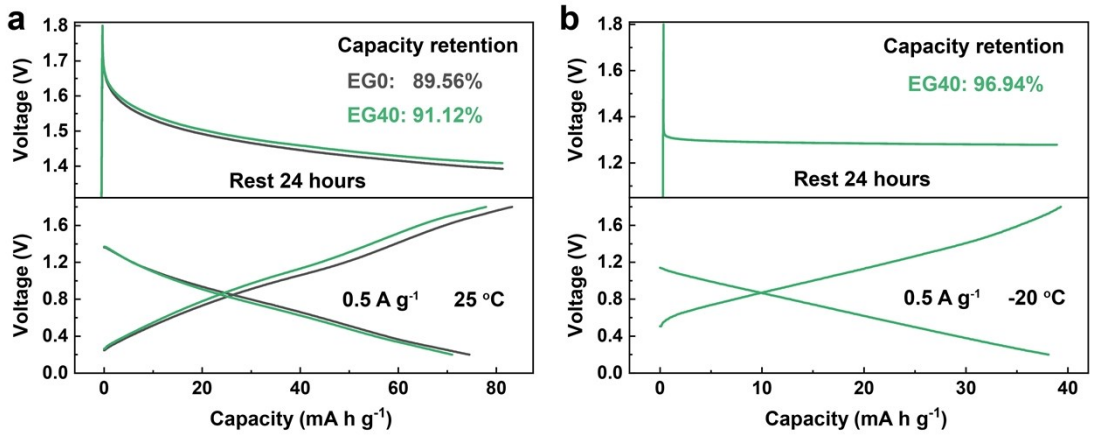

Figure S21. Self-discharge behavior of ZHSCs with EG0 and EG40 after resting 24 hours at (a) 25 °C and (b) -20 °C.

As a result, the ZHSC with EG40 keeps a higher capacity retention of 91.12% than EG0 (89.56%) after resting 24 hours at 25 °C. This indicates that the ZHSC with EG40 exhibits less self-discharge than EG0, probably resulting from the fact that EG impacts the adsorbed state of Zn^{2+} on the surface of cathode. Besides, the higher capacity retention of 96.94% for EG40 after resting 24 hours at -20 °C further confirms the low self-discharge behavior of the ZHSC cells in hybrid electrolytes.

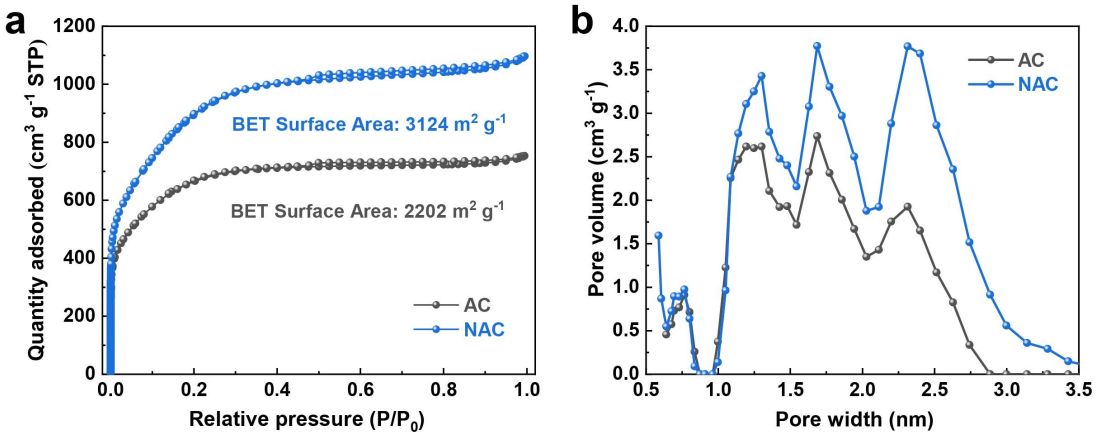

Figure S22. (a) The absorption/desorption isotherms of AC and NAC materials. (b) The pore size distribution of AC and NAC materials.

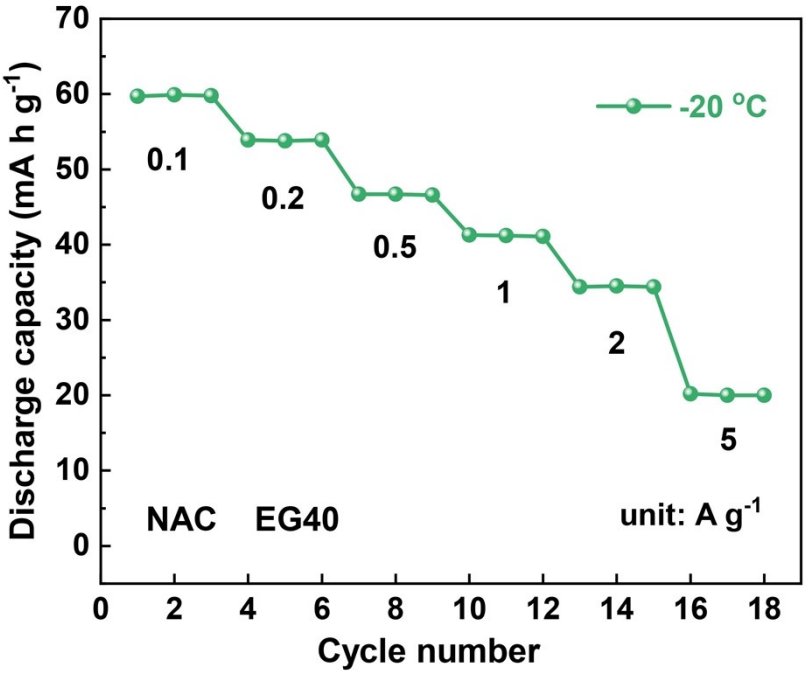

Figure S23. Rate performance of ZHSC with NAC cathode and EG40 electrolyte at -20 °C.

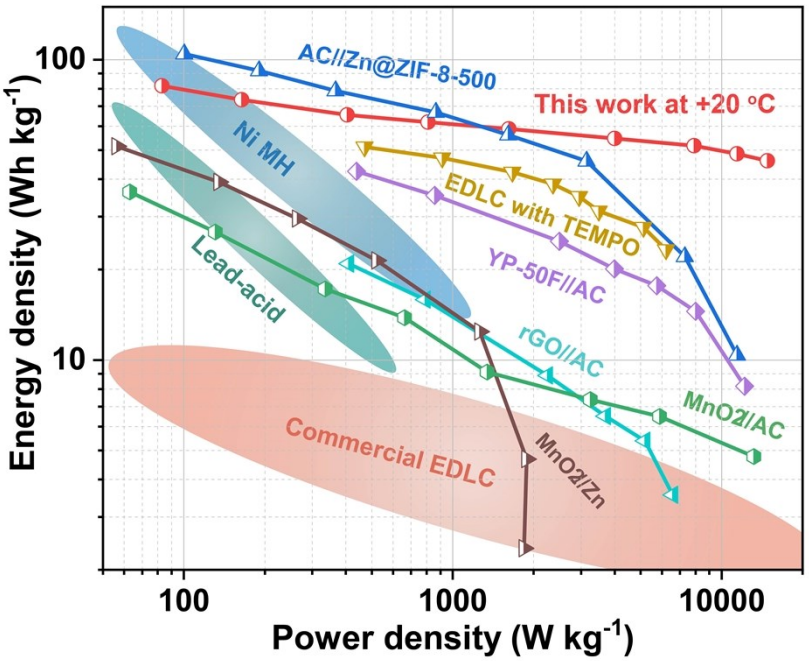

Figure S24. Ragone plot of NAC-EG40 ZHSC in comparison to other carbon-based hybrid devices and some commercial energy storage devices.[33-37]

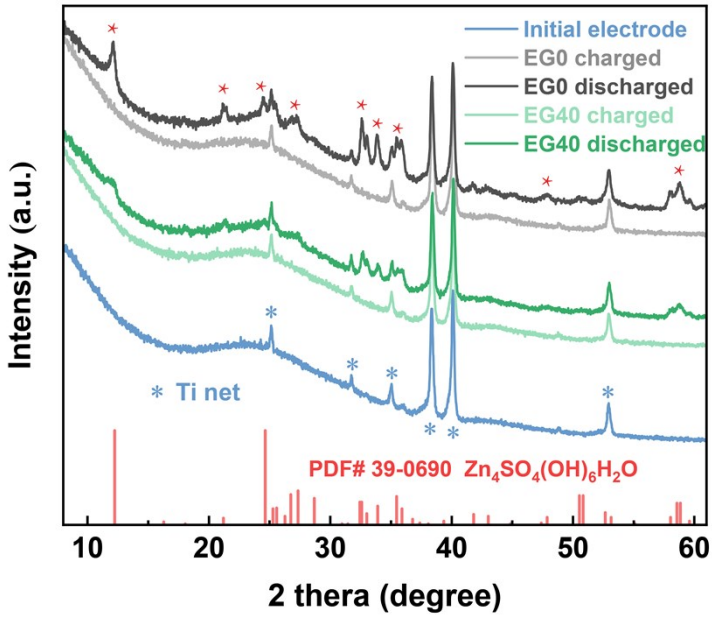

Figure S25. XRD patterns of AC cathode at initial, fully-charged, and fully-discharged states.

Figure S25 shows the XRD patterns of AC cathode after the ZHSC was charged to 1.8 V or discharged to 0.2 V. At fully-discharged state, dominant component of the cathode in EG0 or EG40 is $Zn_4SO_4(OH)_6H_2O$ (JCPDS#39-0690). According to previous research, this discharging product results from the increased pH of the electrolyte caused by the hydrogen evolution reaction (HER) on anode side. Also, the formation-dissolution of $Zn_4SO_4(OH)_6H_2O$ is partially irreversible, thus leading to the rapid capacity decay. Therefore, the amount of $Zn_4SO_4(OH)_6H_2O$ on AC surface to some extent indicates the degree of HER. Interestingly, the peak of $Zn_4SO_4(OH)_6H_2O$ on discharged AC cathode in EG40 is obviously weaker than that in EG0, implying that EG can effectively decrease the side reaction on AC cathode by impacting the solvation state of Zn^{2+} in hybrid electrolytes.

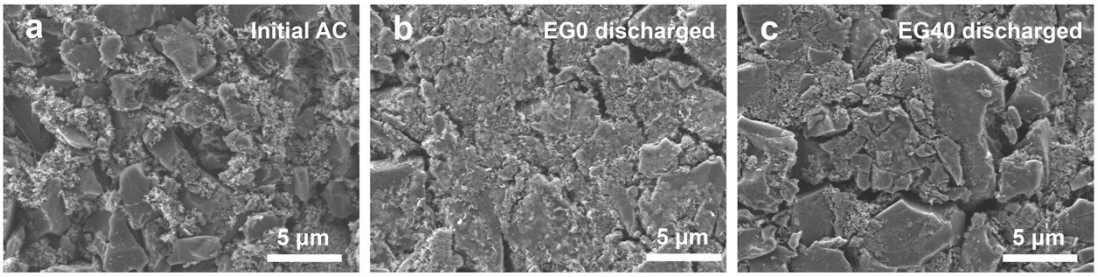

Figure S26. SEM images of AC cathode at (a) initial state, (b) fully-discharged state in EG0, and (c) fully-discharged state in EG40.

As shown in Figure S26, a layer of sheet-like $Zn_4SO_4(OH)_6H_2O$ was observed on the surface of AC cathode discharged within EG0; however, there was no evident product on the AC cathode discharged within EG40. These morphologies suggest that the interfacial side reactions on AC cathode can be greatly declined in hybrid electrolytes.

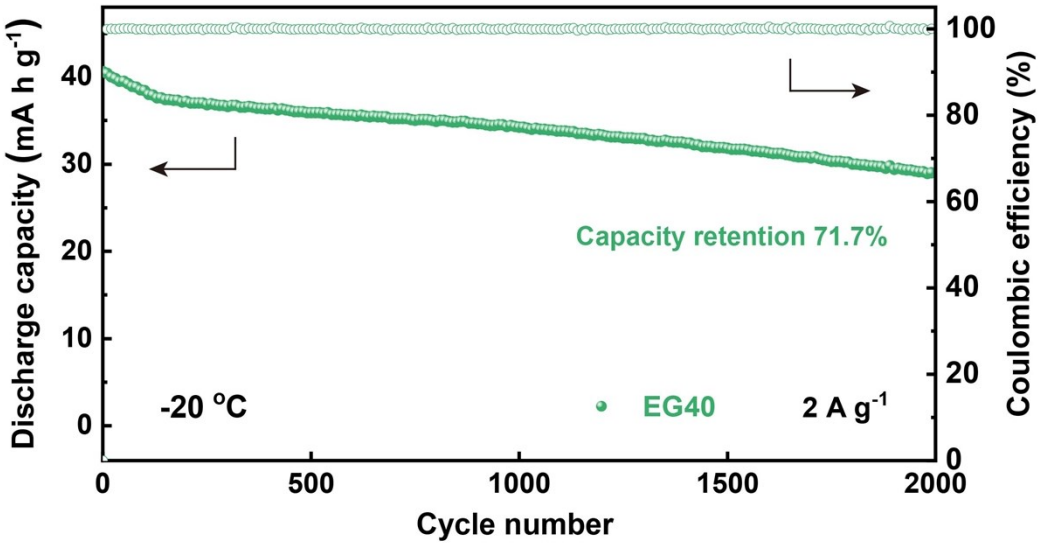

Figure S27. Cycling stability of ZHSC with NAC-EG40 at a current density of 2 A g^{-1} at -20 °C.

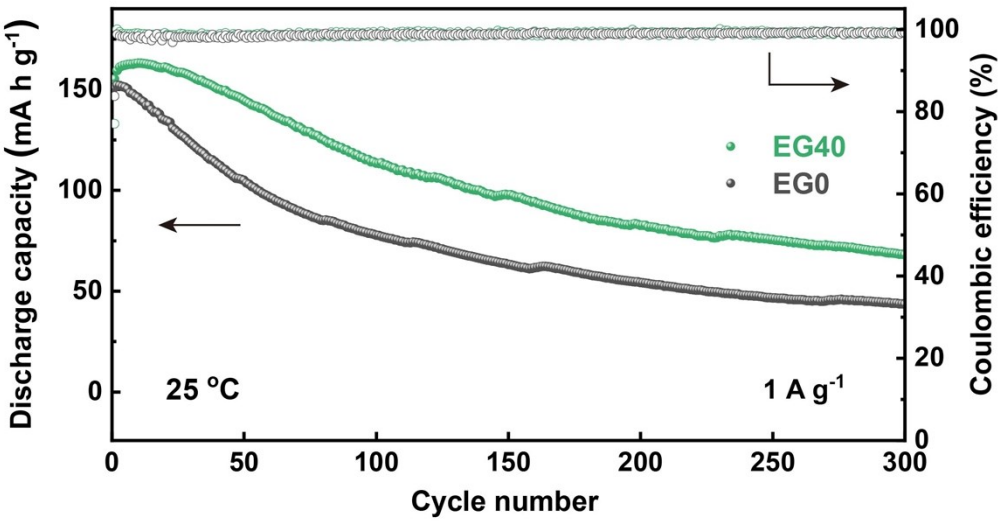

Figure S28. Cycling performance collected at 1 A g^{-1} of the Zn//PANI-V_2O_5 batteries with EG0 and EG40 at 25 ^oC.

In Figure S28, the Zn//PANI-V_2O_5 battery with EG40 exhibits a higher capacity retention than EG0 after 300 cycles, implying that EG to some extent improves the cycling stability of PANI-V_2O_5 materials. However, the Zn//PANI-V_2O_5 battery with EG40 displays an inferior cycling stability at 25 ^oC than that at -20 ^oC. This could be explained by the fact that the solvation interaction of Zn^{2+} with EG exerts more prominent role in the Zn^{2+}-intercalation/deintercalation process especially at low temperature, which has been confirmed by the higher CE of Ti||Zn cells at -20 ^oC than that at 20 ^oC (Figure S15 and S16).

References

1. B. N. Choi, J. H. Yang, Y. S. Kim and C.-H. Chung, *RSC Adv.*, 2019, **9**, 21760-21770.

2. J. Wang, J. Polleux, J. Lim and B. Dunn, *J. Phys. Chem. C*, 2007, **111**, 14925-14931.

3. S. Plimpton, *J.Comput.Phys.*, 1995, **117**, 1-19.

4. W. L. Jorgensen, D. S. Maxwell and J. Tirado-Rives, *J. Am. Chem. Soc.*, 1996, **118**, 11225-11236.

5. J. P. Ryckaert, G. Ciccotti and H. J. C. Berendsen, *J. Comput. Phys.*, 1977, **23**, 327-341.

6. R. W. Hockney and J. W. Eastwood, *Computer Simulation Using Particles*, Routledge, London, England **1989**.

7. S. Nosé, *J. Chem. Phys.*, 1984, **81**, 511.

8. W. G. Hoover, *Phys. Rev. A*, 1985, **31**, 1695-1697.

9. H. J. C. Berendsen, J. P. M. Postma, W. F. van Gunsteren, A. DiNola and J. R. Haak, *J. Chem. Phys.*, 1984, **81**, 3684.

10. C. Adamo, G. E. Scuseria and V. Barone, *J. Chem. Phys.*, 1999, **111**, 2889-2899.

11. F. Weigend and R. Ahlrichs, *Phys. Chem. Chem. Phys.*, 2005, **7**, 3297-3305.

12. M. J. Frisch and E. N. Brothers,, *Journal*, 2016.

13. S. Grimme, S. Ehrlich and L. Goerigk, *J. Comput. Phys.*, 2011, **32**, 1456-1465.

14. S. Grimme, *J. Comput. Phys.*, 2004, **25**, 1463-1473.

15. A. V. Marenich, C. J. Cramer and D. G. Truhlar, *J.Phys. Chem. B*, 2009, **113**, 6378-6396.

16. T. Lu and F. Chen, *J.Comput. Chem.*, 2012, **33**, 580-592.

17. W. Humphrey, A. Dalke and K. Schulten, *J. Mol. Graphics*, 1996, **14**, 33-38.

18. M. Dahbi, F. Ghamouss, F. Tran-Van, D. Lemordant and M. Anouti, *J. Power Sources*, 2011, **196**, 9743-9750.

19. Q. Nian, J. Wang, S. Liu, T. Sun, S. Zheng, Y. Zhang, Z. Tao and J. Chen, *Angew. Chem. Int. Ed.*, 2019, **131**, 17150-17155.

20. Y. K. Ning, Y. U. Bi-Tao, L. I. Fu-Shen and W. H. Qiu, *Electrochemistry*, 2006,

12, 257-261.

21. E. J. Brandon, W. C. West, M. C. Smart, L. D. Whitcanack and G. A. Plett, *J. Power Sources*, 2007, **170**, 225-232.

22. S. Paez and M. Contreras, *J. Chem. Eng. Data*, 1989, **34**, 455-459.

23. I. N. Daniels, Z. Wang and B. B. Laird, *J.Phys. Chem.C*, 2017, **121**, 1025-1031.

24. Y. You, H. R. Yao, S. Xin, Y. X. Yin, T. T. Zuo, C. P. Yang, Y. G. Guo, Y. Cui, L. J. Wan and J. B. Goodenough, *Adv. Mater.*, 2016, **28**, 7243-7248.

25. Y. Yokoyama, H. Uekusa and Y. Ohashi, *Chem. lett.*, 1996, **25**, 443-444.

26. Broughton and G., *J. Am. Chem. Soc.*, **76**, 634-634.

27. X. Dong, Z. Guo, Z. Guo, Y. Wang and Y. Xia, *Joule*, 2018, **2**, 902-913.

28. J. M. Kuchta, A. L. Furno, A. Bartkowiak and G. H. Martindill, *J. Chem. Eng. Data*, 1968, **13**, 421-428.

29. K. M. Abraham and M. Alamgir, *J. Electrochem. Soc.* 1987, **134**, 258-259.

30. C. A. Paddon, S. E. W. Jones, F. L. Bhatti, T. J. Donohoe and R. G. Compton, *J. Phys. Org. Chem.*, 2007, **20**, 677-684.

31. M. Postigo, A. Mariano, L. Mussari, A. Camacho and J. Urieta, *Fluid Phase Equilib.*, 2003, **207**, 193-207.

32. J. Wang, J. Polleux, J. Lim and B. Dunn, *J. Phys. Chem. C*, 2007, **111**, 14925-14931.

33. Z. Wang, J. Huang, Z. Guo, X. Dong, Y. Liu, Y. Wang and Y. Xia, *Joule*, 2019, **3**, 1289-1300.

34. L. Dong, X. Ma, Y. Li, L. Zhao, W. Liu, J. Cheng, C. Xu, B. Li, Q.-H. Yang and F. Kang, *Energy Storage Mater.*, 2018, **13**, 96-102.

35. L. Hu, C. Shi, K. Guo, T. Zhai, H. Li and Y. Wang, *Angew. Chem. Int. Ed.*, 2018, **57**, 8214-8218.

36. X. Ma, J. Cheng, L. Dong, W. Liu, J. Mou, L. Zhao, J. Wang, D. Ren, J. Wu, C. Xu and F. Kang, *Energy Storage Mater.*, 2019, **20**, 335-342.

37. H. Wang, M. Wang and Y. Tang, *Energy Storage Mater.*, 2018, **13**, 1-7.